Spatial Transcriptomics in Mechanomics:

New Horizons in Exploring the Mechanoregulation of Bone Regeneration.

Neashan Mathavan[1], Amit Singh[1], Francisco Correia Marques[1], Denise Günther[1], Gisela Kuhn[1], Esther Wehrle[1, 2†], Ralph Müller[1†]*

[1]Institute for Biomechanics, ETH Zürich, Zürich, Switzerland.

[2]AO Research Institute Davos, Davos Platz, Switzerland.

[†]These authors contributed equally to this work.

Corresponding author: Prof. Ralph Müller, PhD.

Email: ram@ethz.ch

Abstract

In over 100 years, the field of bone mechanobiology has sought experimental techniques to unravel the molecular mechanisms governing the phenomenon of mechanically-regulated bone (re)modelling. Each cell within a fracture site resides within different local micro-environments characterized by different levels of mechanical strain - thus, preserving the spatial location of each cell is critical in relating cellular responses to mechanical stimuli. Our spatial transcriptomics based "mechanomics" platform facilitates spatially-resolved analysis of the molecular profiles of cells with respect to their local *in vivo* mechanical environment by integrating time-lapsed *in vivo* micro-computed tomography, spatial transcriptomics, and micro-finite element analysis. We investigate the transcriptomic responses of cells as a function of the local strain magnitude by identifying the differential expression of genes in regions of high and low strain within a fracture site. Our platform thus has the potential to address fundamental open questions within the field and identify novel mechano-responsive targets to enhance bone regeneration.

Teaser

A spatial omics platform to investigate the intricate molecular orchestration of mechanically-regulated bone regeneration.

Introduction

In the late 19th century, the German orthopedic surgeon Julius Wolff established the fundamental principle of bone mechanobiology by describing the dynamic nature of bones and their remarkable ability to adapt to their mechanical environment (*1*). This principle underscores the critical importance of the mechanical environment to the regenerative capacity of bone. Mechanical stimuli can either enhance or impair the regenerative process (*2*). At its core, the mechanobiology of bone regeneration is governed by the response of cells at the fracture site to physical stimuli. However, it has proven extremely difficult to investigate the transduction of mechanical stimuli exerted at the organ level to site-specific cellular responses at the molecular level. Despite considerable advances in recent decades (*3*, *4*), our understanding of the specific signaling pathways underlying the mechanoregulation of bone regeneration remains in its nascent stages.

Each cell within a fracture site resides within different local micro-environments characterized by different levels of mechanical strain. The challenge within the field has been the need for more integrative approaches to investigate the multi-scale regenerative response of individual cells in response to their local *in vivo* mechanical environment (*5*). Insights into this critical missing link have the potential to be transformative within the field by greatly improving our ability to anticipate cellular responses to different magnitudes or modes of mechanical stimuli. In pursuing the characterization of cellular activity as a function of its local *in vivo* mechanical environment, experimental approaches have largely been confined to *in vitro* (*6*) and *in silico* (*5*) techniques. The challenges with *in vivo* approaches are significant. Rodent fracture models (*2*), osteogenic loading protocols (*7*) and *in vivo* imaging techniques (time-lapsed micro-computed tomography, micro-CT) (*8*) are well-established within the field. However, *in vivo* mechanical loading applied at the organ scale is heterogeneously distributed throughout the fracture site, resulting in complex mechanical environments with distinct regions of high and low strain. Spatial correlation is thus required to associate cellular responses with their respective local *in vivo*

mechanical environments. Currently, micro-finite element analysis (micro-FE) is the only established technique available to generate 3D maps of the *in vivo* mechanical environment. High-resolution micro-FE models derived from micro-CT images of the fracture site have been used to associate morphological changes at the tissue scale with the local mechanical environment (*9*). Moreover, osteocytes – the primary mechanosensory cell in bone and constituting > 90% of all bone cells – reside deep within the bone matrix. Direct experimental observation of these cells is thus challenging without destruction of or interference with the surrounding tissue environment. Techniques such as laser capture microdissection, in combination with FE modelling, have permitted "mechanomic" analyses of a small number of isolated cells (*5*). In contrast, recent advances in spatially resolved "omics" technologies now permit the comprehensive, unbiased mapping of molecular pathways and cellular function within the spatial context of complex tissue architectures (*10*). However, the use of these technologies in bone has been limited due to the calcified nature of the tissue.

To investigate the molecular responses of cells to their local mechanical environment within a mechanically loaded fracture site, we have established a spatial-transcriptomics based "mechanomics" platform (Figure 1). Spatial transcriptomics – a recent, transformative advancement in cellular profiling technologies – permits characterization of the transcriptomic responses of cells within their native spatial context on histology sections. Our platform consists of: (i) an established femur defect mouse model (*11*), (ii) established *in vivo* micro-CT imaging protocols and analyses (*9*), (iii) an established osteogenic cyclic mechanical loading protocol (*11*, *12*), (iv) an established spatial transcriptomics protocol for bone tissue (*13*) and (v) an established *in silico* micro-FE modelling approach (*12*). Our objective is to demonstrate the potential of a spatial transcriptomics-based "mechanomics" platform to identify the molecular mechanisms governing the mechanoregulation of bone regeneration. As illustrated in Figure 1, we introduced femoral osteotomies in mice and performed weekly *in vivo* micro-CT imaging of the fracture sites.

Following bridging of the fracture site at 3 weeks post-surgery, the mice were subdivided into Control and Loaded groups and received either sham loading or cyclic mechanical loading. We first quantified the effects of mechanical loading using micro-CT-derived bone morphometric indices and visualized the sites of bone formation, quiescence and resorption. Next, we corroborated our findings by comparing the transcriptomic responses in Control vs. Loaded fracture sites. To correlate spatially resolved gene expression profiles with their local *in vivo* mechanical environments, we analyzed the transcriptomic profiles at sites of high strain and low strain within a mechanically loaded fracture site. Finally, we assessed the merits of our spatial mechanomics platform and its potential to develop a molecular-based understanding of the local mechanoregulation of bone regeneration.

Results

Micro-CT-based bone morphometric analysis underscores a strong anabolic response to cyclic mechanical loading

Time-lapsed *in vivo* imaging permits visualization of the sites of bone formation, quiescence and resorption at the fracture site as shown at weekly intervals in Figure 2. Comparable healing responses were observed between Control and Loaded fracture sites between weeks 0 – 3. This was reinforced by comparing bone morphometric parameters between weeks 0 – 3 across all volumes of interest (Figure 2 [A] – [H]). Upon bridging at week 3, the fracture sites of Loaded mice were subjected to cyclic mechanical loading 3 times per week. Loading induced a strong anabolic response as can be observed in Figure 2 where sites of bone formation (in orange) predominate at the loaded fracture site between weeks 3 - 5. In contrast, the fracture sites of Control mice were observed to undergo remodeling during the same period (Figure 2). In comparisons of bone morphometric parameters, cyclic mechanical loading was found to induce significantly larger callus / bone volume formation (data represented as mean ±SD). At week 5, BV/TV in the defect center was 40.9 ±0.8% in Control mice vs. 70.8 ±6.5% in Loaded mice (Figure 2[A]). Similarly, in the

defect periphery, BV/TV was 14.1 ±3.8% in Control mice vs. 31.9 ±9.4% in Loaded mice (Figure 2[B]). At week 5, loading induced an increased rate of bone formation (0.73 ±0.2% per day in Control mice vs. 1.67 ±0.3% per day in Loaded mice) and a diminished rate of bone resorption (-0.71 ±0.2% per day in Control mice vs. -0.11 ±0.0% per day in Loaded mice) in the defect center (Figure 2[E]). Similarly, in the defect periphery, loading induced an increased rate of bone formation (0.22 ±0.0% per day in Control mice vs. 1.60 ±0.2% per day in Loaded mice) and a diminished rate of bone resorption (-0.45 ±0.3% per day in Control mice vs. -0.05 ±0.0% per day in Loaded mice) (Figure 2[F]).

Significantly enhanced osteogenic response corroborated by spatial analyses of differential gene expression

Spatial analyses of differential gene expression (DEG) in bone regions at the fracture sites of Control and Loaded mice revealed significantly higher expression of osteogenic markers in response to mechanical loading (Figures 4-5). Regions for the analysis were defined by selecting spots in each histological section encompassing all bone spots at the fracture site between the two inner pins of the external fixator (Figure 5[A]). Quality control measures for these bone regions were as follows: the median number of unique molecular identifiers (UMIs) for the Control and Loaded sections were 3602 and 2708 respectively, and the median number of unique genes for the Control and Loaded sections were 2670 and 1924 respectively. In these defined bone regions of the fracture site, 9889 genes were identified with sufficiently high expression to be included in the DEG analysis. Of these, 1139 genes were differentially expressed (FDR-adjusted p value cutoff < 0.1; absolute log2 fold change > 0.5) with 524 genes upregulated and 615 genes downregulated [Supplementary Table 2]. To present differential gene expression in subsequent sections, the following convention is used: *Gene* (+/- log2 fold change).

Significantly higher expression of markers of osteoblast differentiation and osteoblast activity were present in response to loading: *Bglap* (+3.3 fold), *Alpl* (+2.3 fold), *Sp7* (+1.7 fold), *Col1a1* (+1.5 fold), *Col1a2* (+1.5 fold), and *Runx2* (+0.9 fold) (Figure 5[B][C]; Supplementary Table 2). Visualization of the spatial expression of these genes further underscored this result (Figure 4 [A] – [D]). Markers of mineralizing osteocytes: *Phex* (+4.1 fold), *Dmp1* (+2.7 fold), and mature osteocytes: *Mepe* (+3.9 fold), *Sost* (+2.2 fold) were also upregulated (Figure 4 [E] – [G]; Figure 5[B][C]). Furthermore, amongst the top-ranked upregulated genes include genes associated with osteogenesis (*14*): *Wnt7b* (+3.4 fold), endochondral ossification (*15*, *16*): *Adam12* (+3.7 fold), matrix synthesis (*17*): *Cdo1* (+4.4 fold), and mineralization (*18–20*): *Car12* (+19.4 fold), *Smpd3* (+17.9 fold) and *Phospho1* (+2.2 fold) (Figure 5[B][C]; Supplementary Table 2).

Coincident with this enhanced osteogenic response, *Ccn2* (-3.7 fold) – a master regulator of osteogenesis and chondrogenesis (*21*), *Nbl1* (-2.1 fold) – a BMP-antagonist (*22*), and *Mgp* (-1.4 fold) – a potent mineralization inhibitor (*23*, *24*), were downregulated (Figure 5[B]; Supplementary Table 2). Osteoclast markers were less prominent in the results with expression of *Ctsk* and *Acp5* not significantly different between Control and Loaded fracture sites and upregulation of genes associated with osteoclastogenesis (*25*, *26*) and osteoclast activity (*26–29*): *s100a8* (+2.3 fold), *Ncf1* (+1.6 fold) and *Mmp9* (+0.8 fold) (Figure 4 [H] – [J]; Figure 5[B][C]; Supplementary Table 2).

Known mechano-responsive genes were also present amongst the top-ranked genes including: *Il11* (+17.5 fold) – a cytokine predominantly expressed in bone (*30*, *31*), *Ccn2* (-3.7 fold) (*21*, *32*), *Wnt7b* (+3.4 fold) (*33*, *34*), *Sost* (+2.2 fold) – a Wnt-antagonist (*35*, *36*), *Gja1* (+2.0 fold) – which encodes for the gap junction protein connexin 43 (*37*), *Sfrp4* (-1.4 fold) – a Wnt-antagonist (*38–40*), and *Cdkn1a* (-0.7 fold) – a negative regulator of osteogenesis (*41*, *42*) (Figure 5[B][C]; Supplementary Table 2).

Mechanomics analyses reveal regions of high / low strain are associated with sites where bone formation / resorption responses respectively predominate

In the Loaded spatial transcriptomics section, gene expression profiles corresponding to high strain (> 1000 με, n = 22 spots), low strain (< 500 με, n = 24 spots) and reference strain regions (> 500 με and < 1000 με, n = 42 spots) were analyzed (Figure 7). Using the co-efficient of variance (CV) as a measure of functional significance, the top-ranked genes in regions of high strain included genes associated with an anabolic response: *Spp1*, *Col1a2*, *Col1a1*, *Bglap*, *Sparc*, *Col11a2*, *Gpx3*, *Pdia3* (*43*), the osteoclastogenesis inhibitor (*44*): *Cd74* and the mineralization inhibitor: *Mgp* (Figure 8[A]). In contrast, the top-ranked genes in regions of low strain included genes associated with a catabolic response: *S100a8*, *Mmp9*, *Tpm1* (*45*, *46*), *Ctsk*, *Ncf1* and *Igfbp4* (*47*, *48*) (Figure 8[A]). In the reference strain region, the top-ranked genes included genes associated with an anabolic response: *Spp1*, *Sparc*, *Bglap*; genes associated with a catabolic response: *Ctsk*, *Acp5*, *Mmp9*; and genes which couple bone formation with resorption: *Mmp13* (*27*) (Figure 8[A]).

In comparisons of high strain vs. reference strain regions, 5146 genes were identified with sufficiently high expression to be included in a DEG analysis. Of these, 161 genes were differentially expressed (FDR-adjusted p value cutoff < 0.1; absolute log2 fold change > 0.5) with 150 genes upregulated and 11 genes downregulated [Supplementary Table 3]. The following genes associated with bone formation were found to be upregulated: *Coq10a* (+2.2 fold) (*49*, *50*), *Myh2* (+2.0 fold) (*51*), *Sirt7* (+1.9 fold) (*52*), *Sod2* (+1.5 fold) (*53*), *Pdia3* (+1.0 fold) and *Col1a2* (+0.9 fold) (Figure 8[B]; Supplementary Table 3). All remaining upregulated genes had no established roles in bone function or are ubiquitously expressed. Downregulated genes included the following genes associated with bone mineralization: *Alpl* (-1.4 fold), *Sparc* (-0.8 fold); and the following genes associated with bone resorption: *Jdp2* (-1.6 fold) (*54*), *Snai1* (-1.5 fold) (*55*, *56*), *Mmp9* (-1.5 fold), *Acp5* (-1.4 fold), *Myh9* (-1.4 fold) (*57*, *58*) and *Ctsk* (-0.9 fold) (Figure 8[B]; Supplementary Table 3). All remaining downregulated genes had no established roles in bone function. Gene-set

enrichment analysis of differentially expressed genes identified the positive enrichment of signaling pathways associated with bone formation (FDR-adjusted p value < 0.05) (Figure 8[C]; Supplementary Table 5).

In comparisons of low strain vs. reference strain regions, 5146 genes were identified with sufficiently high expression to be included in a DEG analysis. Of these, 40 genes were differentially expressed (FDR-adjusted p value cutoff < 0.1; absolute log2 fold change > 0.5) with 9 genes upregulated and 31 genes downregulated [Supplementary Table 4]. The following genes associated with bone resorption were found to be upregulated: *S100a8* (+1.5 fold), *Ncf1* (+1.2 fold) and *S100a9* (+1.0 fold) (Figure 8[B]; Supplementary Table 4). All remaining upregulated genes had no established roles in bone function or are ubiquitously expressed. Downregulated genes included the following genes associated with bone formation: *Mmp2* (-1.3 fold), *Bglap* (-1.3 fold), *Sparc* (-1.2 fold), *Gpx3* (-1.1 fold) (*59*), *Spp1* (-1.0 fold), *Serpinh1* (-1.0 fold) (*60*) and *Col3a1* (-0.6 fold); the following negative regulators of osteogenesis: *Cdkn1a* (-1.2 fold) and *Fgfr1* (-1.2 fold) (*61*, *62*); and the following genes associated with bone resorption: *Acp5* (-1.3 fold), *Fgfr1* (-1.2 fold) (*63*), *Rack1* (-0.9 fold) (*64*), *Tpm1* (-0.7 fold) and *Ctsk* (-0.7 fold) (Figure 8[B]; Supplementary Table 4). All remaining downregulated genes had no established roles in bone function.

Discussion

The mechano-responsiveness of bone cells has been recognized for over 100 years, yet the underlying biological mechanisms remain not well understood. It has proven extremely difficult to investigate the role of local mechanical environments at fracture sites in driving site-specific cellular responses. In this study, we address this challenge by demonstrating the potential of our spatial transcriptomics based “mechanomics” platform in exploring the mechanoregulation of bone regeneration. Using an established femur defect mouse model, we demonstrate that our cyclic mechanical loading protocol induces a strong anabolic response corroborated by time-lapsed micro-

CT measurements and spatial transcriptomics profiling. Moreover, in associating gene expression profiles with their local mechanical environments, sites of high strain were associated with bone formation responses and sites of low strain were associated with bone resorption responses. Our spatial transcriptomics-based "mechanomics" platform thus presents new opportunities to investigate fundamental questions within the field of bone mechanobiology.

Micro-CT-based bone morphometric analysis confirmed the effect of cyclic mechanical loading with a significantly enhanced osteogenic response producing much larger callus / bone volumes. Although limited to n = 2 mice per group, this is corroborated by our previous studies in female 20-week-old C57BL/6 mice (*11*), female 12-week-old and 35-week-old PolgA$^{D257A/D257A}$ mice (*65*, *66*) and female 12-week-old BCR:PolgA $^{D257A/D257A}$ mice (*67*). Moreover, as illustrated in Figure 2, sites of bone formation (identified in orange) unequivocally predominate between weeks 3 – 5 in the mechanically loaded fracture sites.

Visualization of spatial gene expression at the fracture sites and differential gene expression analyses further underscored this osteogenic effect with upregulation of genes associated with matrix synthesis (*Col1a1*, *Col1a2* and the non-collagenous proteins: *Bglap*, *Sp7*) and mineralization (*Alpl*, *Dmp1*, *Phex*, *Car12*, *Smpd3*, *Phospho1*) (Figure 5[B][C]; Supplementary Table 2). Despite the functional importance of members of the tumor necrosis family, significant differences in the expression of osteoprotegerin (OPG – encoded by *Tnfrsf11b*) and receptor activator of nuclear factor kappa-B ligand (RANKL – encoded by *Tnfsf11*) were not present. Elevated expression of both OPG and RANKL has been reported in a tibial closed-fracture mouse model with levels gradually subsiding over a 4-week period relative to contralateral control tibias (*68*). However, in the present study, mechanical loading of the fracture site did not markedly alter the expression of OPG – an inhibitor of osteoclastogenesis. In agreement, markers of osteoclastogenesis (*Ncf1*, *Mmp9*) were found to be upregulated, and are likely the result of the coupling of the anabolic and catabolic phases of the response to mechanical loading.

The prevalence of osteocyte markers (*Phex*, *Dmp1*, *Mepe*, *Sost*) amongst the top differentially expressed genes is noteworthy and likely reflect the following processes at the fracture site: (i) mineralization driven by young osteocytes (*Phex*, *Dmp1*), (ii) regulation of mineralization by mature osteocytes (*Mepe*), and (iii) the progressive maturation of osteocytes encapsulated in the bone matrix (*Mepe*, *Sost*) (*69*). The upregulation of *Sost* – a potent inhibitor of Wnt signaling in osteoblasts – was unexpected. The expression of *Sost* is regulated by both biochemical (*70*, *71*) and mechanical (*36*) cues. In intact bones, *Sost* expression is downregulated with mechanical loading and upregulated with mechanical unloading (*36*). However, fewer studies have investigated the role of *Sost* in the context of bone regeneration. Coates et al. conducted a comparison of the transcriptional profiles of intramembranous and endochondral ossification following fracture (*72*). In their model of intramembranous ossification in the mouse ulna, *Sost* was downregulated at 4 hours and 1 day following fracture relative to the intact contralateral ulna. In their model of endochondral ossification in the mouse femur, *Sost* was downregulated at 4 hours, 1 day, 3 days, 7 days and 14 days following fracture relative to the intact contralateral femur. The bone formation mechanism (that is, intramembranous vs. endochondral ossification) within each of these models is determined by the mechanical stability of the injury site. This demonstrates that the regulation of *Sost* at fracture sites is not exclusively mechanical in nature. Moreover, Kruck et al. investigated the efficacy of sclerostin neutralizing antibody (SclAb) on the regeneration process in a mouse femur fracture model (*73*). Notably, *Sost* and sclerostin expression at both the gene and protein level respectively, were upregulated following SclAb administration. The authors concluded that this increased sclerostin expression may be the result of a yet unknown negative feedback mechanism. The upregulation of *Sost* following mechanical loading presented in this publication may thus reflect this negative feedback mechanism given the strong osteogenic response induced by mechanical loading and thus warrants further investigation.

In associating molecular pathways at the cellular scale with their local mechanical *in vivo* environment within a single histological section, cells in regions of high strain were found to express genes involved in bone formation responses: upregulation of *Coq10a*, *Myh2*, *Sirt7*, *Pdia3* and *Col1a2*, downregulation of *Jdp2*, *Snai1*, *Mmp9*, *Acp5*, *Myh9* and *Ctsk*, and positive enrichment of "*osteoblast development*", "*ossification*", "*positive regulation of Wnt signaling pathway*" and "*negative regulation of hippo signaling*"; whereas cells in regions of low strain were found to express genes involved in bone resorptive responses: upregulation of *S100a8*, *Ncf1* and *S100a9* and downregulation of *Mmp2*, *Bglap*, *Sparc*, *Gpx3*, *Spp1* and *Serpinh1*. This finding is in agreement with the fundamental principle of Wolff's Law on the capacity of bone to functionally adapt to its mechanical environment. However, we are yet to establish the mechanobiological mechanisms governing these strain-specific cellular responses as this would necessitate a more comprehensive dataset. Indeed, it cannot be ruled out that the cellular responses observed are (to a partial extent) site-specific responses or biochemically-driven responses independent of the local mechanical environment. Nevertheless, this demonstration within a single histological section of bone underscores the potential of our platform to develop a molecular based understanding of the mechanoregulation of bone regeneration. Indeed, the ability to analyze spatially-resolved omics data with respect to the local *in vivo* mechanical environment is a significant achievement within the field of bone mechanobiology.

In assessing the merits of our platform, novel features, opportunities for further optimization and limitations were considered. The spatially resolved characterization of the transcriptome of a fracture site presented herein is a notable feature. Historically, experimental methodologies within the field have presented a trade-off between the use of omics technologies to sequence the genome, transcriptome or proteome from dissociated specimens vs. the use of immunohistochemistry or *in situ* hybridization to localize a predetermined subset of molecules within intact tissues. With the advent of spatial molecular profiling technologies, spatially contextualized maps of the diverse

landscape of cell types and their functions can be captured. However, the use of spatial transcriptomics in bone presents challenges due to the mineralized nature of bone. The need to maintain a delicate balance between tissue decalcification and RNA preservation has constrained the use of spatial transcriptomics in bone studies. However, we have established and made available a protocol for the use of the Visium Spatial Gene Expression assay with FFPE bone sections (*13*). The success of our protocol is evident in quality control measures. In measures of both unique transcripts and unique genes, the median numbers for our data were notably higher than those reported for bone sections in the literature (*74*). Although beyond the scope of this publication, our experiments with the Visium Spatial Gene Expression assay also permitted preservation of muscle and marrow at the fracture site. The technique thus provides new avenues to investigate the crosstalk between different cell populations and its roles in driving the regenerative response at the fracture site. Notably, genes without well-defined roles in bone regeneration also featured prominently in our differential gene expression analyses underscoring the transformative potential of spatial profiling technologies in unravelling molecular pathways and mechanisms.

The platform does present opportunities for further optimization and is not without limitations. To associate transcriptomic responses of cells to their local *in vivo* mechanical environment, a 2D histological section was visually aligned within the 3D micro-CT derived mechanical environment. However, the use of an approach based on visual assessment is both labor intensive and error prone. Machine learning driven 2D-to-3D registration techniques can potentially be incorporated into the platform to perform this task. Moreover, the transcriptomics data generated using the Visium Spatial Gene Expression assay is not at single-cell resolution. Instead, the capture area on each Visium slide consists of a grid of 55 µm diameter spots with the center of each spot positioned approximately 100 µm from the center of adjacent spots. Each spot may thus overlap the boundaries between tissue structures or strain regions and may necessitate the exclusion of specific spots. Calluses with trabecular structures pose a specific challenge as the grid pattern of

the Visium capture areas may not be optimally positioned to capture the transcriptomic response within each trabecular strut. Recent advancements in omics technologies have led to the availability of techniques for generating spatially-resolved omics data at single-cell resolution. Integration of such techniques into our platform represents the next logical progression in its evolution. Finally, the RNA quality of transcriptomics data generated from formalin-fixed paraffin embedded samples is generally inferior to fresh frozen samples. Protocols for the use of fresh frozen bone samples with Visium Spatial Gene Expression assay are yet to be established and future applications using our platform should consider the use of fresh frozen samples.

In conclusion, we present an experimental platform to perform spatially-resolved analysis of the transcriptomic responses of cells with respect to their local *in vivo* mechanical environment. Given the limited understanding of the cellular and molecular mechanisms governing the mechanobiology of bone repair, the platform addresses the fundamental open question within the field: Which cell populations and signaling pathways sense and respond to local mechanical stimuli? Insights into the mechanoregulation of bone regeneration will have implications for the broader translation of mechano-therapeutics to clinical settings and it will potentially identify new strategies and novel mechano-responsive targets to enhance regeneration in compromised healing environments.

Materials and Methods

Experimental Design

Our objective is to demonstrate the potential of our spatial-transcriptomics based mechanomics platform in investigating the mechanobiology of bone regeneration. As illustrated in Figure 1, the platform consists of: (i) an established femur defect mouse model (*11*), (ii) established *in vivo* micro-CT imaging protocols and analyses (*9*), (iii) an established osteogenic cyclic mechanical loading approach (*11*, *12*), (iv) an established spatial transcriptomics approach for bone tissue (*13*) and (v) an established *in silico* micro-FE modelling approach (*12*).

Ethics statement

All mouse experiments were performed in accordance with relevant national regulations (Swiss Animal Welfare Act, TSchG, and Swiss Animal Welfare Ordinance, TSchV)) and authorized by the Zürich Cantonal Veterinary Office (approved license number: ZH229/2019; Kantonales Veterinäramt Zürich, Zurich, Switzerland).

Mouse line

Our lab has previously established a bone cell reporter (BCR) mouse model using CRISPR/Cas9 technology to label osteoblast (Integrin binding sialoprotein - Ibsp) and osteoclast-specific targets (tartrate-resistant acid phosphatase (TRAP) type 5 - Acp-5) with fluorescent proteins (eGFP, mCherry) (*75*). All mice were bred, monitored and maintained under specific pathogen free (SPF) conditions at the ETH Phenomics Centre, ETH Zürich (12 h:12 h light-dark cycle, ad libitum access to maintenance feed and water).

Femur defect model

Female 12-week-old BCR mice (n = 4) received mid-diaphyseal femoral defects (0.68 ± 0.04 mm) using an established osteotomy surgical protocol (*11*). Briefly, an external fixator (Mouse ExFix, RISystem, Davos, Switzerland) was positioned at the craniolateral aspect of the right femur using

four mounting pins and the defect was created using a 0.66 mm Gigli wire saw. Pre-operative analgesia (25 mg/L, Tramal®, Gruenenthal GmbH, Aachen, Germany) was provided via the drinking water two days before surgery until the third post-operative day. Anesthesia for all animal procedures (surgery, *in vivo* imaging, mechanical loading) was achieved using isoflurane (induction/maintenance: 5%, 2–3% isoflurane/oxygen).

In vivo micro-CT imaging

In vivo micro-CT imaging of the fracture site between the two inner screws of the external fixator was performed weekly in all mice (weeks 0-5; vivaCT 80, Scanco Medical AG, Brüttisellen, Switzerland) (10.5 µm resolution, 55 kVp, 145 µA, 350 ms integration time, 500 projections per 180°, 21 mm field of view (FOV), scan duration ca. 15 min). To avoid motion artifacts during scanning, a custom-designed holder was used to secure the external fixator (*11*).

Registration of time-lapsed *in vivo* images permits visualization of sites of bone formation, quiescence and resorption (*8*). Reconstructed micro-CT images of each mouse were registered sequentially using an established algorithm (*9*); proximal and distal cortices were registered separately at time-points where bridging of the fracture site was not present as minor relative displacements between proximal and distal cortices were observed to occur. Images were Gaussian filtered (sigma 1.2, support 1) and bone volumes (bone volume—BV) were computed (threshold: 395 mg HA/cm^3) in four non-overlapping volumes of interest (VOIs): the defect center (DC), the defect periphery (DP), the existing fracture cortices together with the medullary cavity (FC) and the cortex periphery (FP) (Figure 3) (*9*). Bone morphometric indices (bone volume/total volume—BV/TV, bone formation rate – BFR, bone resorption rate – BRR) were evaluated within each VOI. Bone volumes were normalized with respect to the central VOIs (DC, FC) which represent the total volume (TV) of intact bone (*9*): thus, DC/DC, DP/DC, FC/FC, FP/FC. Defect sizes (h) were calculated using the following formula: h = 2DC / (CSA_P + CSA_D) where DC is the defect

volume at week 0 and CSA_P and CSA_D represent the proximal and distal cross-sectional areas respectively, which are situated directly adjacent to the fracture site.

Mechanical loading

Following bridging of the fracture site at 3 weeks post-surgery, the mice received either individualized cyclic mechanical loading (*11*, *12*) via the external fixator (n = 2, 8-16N, 10Hz, 3000 cycles) or 0N sham-loading (n = 2). Loading is applied 3 times per week. Detailed descriptions of the protocols can be found in the literature (*11*, *12*). In brief, the mechanical loading applied at each time point is based on computation of the strain distribution within the fracture site of each mouse and the scaling of the strain distribution to achieve a pre-defined median target strain. This is implemented in real-time within a single anesthetic session each week as follows: directly following *in vivo* micro-CT imaging, the CT data is reconstructed and a high-resolution *in silico* finite element (FE) model of the fracture site generated. The FE model simulates axial compression (48-core Intel(R) Xeon(R) Platinum 8168 CPU @ 2.70GHz) and a histogram of the strain distribution is generated. The strain distribution is subsequently scaled by the applied load to achieve a pre-defined median target strain. Furthermore, to assess if the loading poses a structural failure risk at the fracture site, the simulation identifies voxels which exceed more than 10000 με. If more than 100 voxels exceed this threshold, the loading value is reduced by 1N. This optimized load is then applied to the mouse. As the optimized load is based on the *in vivo* micro-CT image and *in silico* simulation at each weekly time-point, loading is individualized to each mouse such that the induced median strain in all loaded mice is of comparable magnitude (*12*).

Spatial transcriptomics

All mice were euthanized at 10 hours following the final cyclic mechanical loading session at 5 weeks post-surgery. Spatially resolved transcriptomics analyses were performed on explanted femurs (n = 1 per group) using the Visium Spatial Gene Expression for formalin-fixed paraffin-embedded (FFPE) assay (10x Genomics, Pleasanton, United States) (*13*). Explanted femurs were

immediately fixed in 10% neutrally buffered formalin for ca. 16 – 24 hours at 4°C, decalcified in 12.5% EDTA (pH 7.5) for 10 days at 4°C, placed in a tissue processor and embedded in paraffin. Protocol details have been published separately using the section from the Control mouse (*13*). To assess the RNA quality, RNA was extracted from each sample (Qiagen RNeasy FFPE Kit, Hilden, Germany) and the DV 200 value (that is, the percentage of total RNA fragments >200 nucleotides) of each sample was evaluated (Agilent 4200 TapeStation, Waldbronn, Germany). As per the manufacturers' instructions, only samples with a DV 200 > 50% were selected for spatial gene expression analyses. 5 µm longitudinal sections from each explanted femur (n = 1 Control, n = 1 Loaded) were placed onto 6.5 x 6.5 mm capture areas on a Visium Spatial Gene Expression slide. Sections were subsequently deparaffinized, subjected to hematoxylin and eosin (H&E) staining, imaged and decrosslinked in accordance with manufacturers' instructions (10x Genomics, CG000409, Rev D). Sections were probe hybridized with 20551 genes targeted (10x Genomics, Visium Mouse Transcriptome Probe Set v1.0) and spatial transcriptomics libraries were prepared. Libraries were sequenced on an Illumina NovaSeq6000 System (Illumina, San Diego, United States) at a sequencing depth of approximately 75 – 120 million reads per sample.

Analysis of sequencing data

Demultiplexing and manual alignment of the sequencing data to the histological image were performed using the SpaceRanger analysis pipeline (10x Genomics, version 2.0.0) and Loupe Browser (10x Genomics, version 6.2.0) respectively. Further downstream data analyses and visualization were performed in R (version 4.3.1) using Seurat (version 4.4.0). Spots were excluded by filtering each sample separately based on the number of UMIs (nCount_Spatial >= 500) and the number of genes (nFeature_Spatial >= 250).

Regions of interest: Regions of interest (ROI) were defined in Loupe Browser by selecting spots which corresponded to specific structures in the H&E stained histological images. Barcodes corresponding to all spots in each region of interest are provided in Supplementary Table 1. In

comparisons between Control and Loaded sections, ROIs were defined at the fracture site encompassing all bone spots between the two middle pins (Figure 5; Control: n = 131 spots, Loaded: n = 146 spots). The entire region between the two middle pins was selected as in the loaded mouse this region is subjected to loading. Furthermore, in the Loaded section, ROIs were defined based on the local mechanical environment: high strain region (> 1000 με), low strain region (< 500 με) and reference strain region (> 500 με and < 1000 με).

Differential gene expression analysis: Differential gene expression analyses were performed using DESeq2 by implementing scaling normalization through deconvolving size factors using scran. In addition, null hypothesis testing was conducted using the likelihood ratio test (*76*). Lists of differentially regulated genes for the different comparisons are provided in Supplementary Tables 2–4. Differentially expressed genes were selected using an FDR-adjusted p value cutoff < 0.1 and an absolute log2 fold change > 0.5. To compare gene expression profiles at sites of high and low strain, the co-efficient of variance (CV) was used to identify genes of functional significance across all spots within a region.

Gene enrichment analysis: Gene-set enrichment analysis was performed using Generally Applicable Gene-set Enrichment (GAGE; Bioconductor version 3.18). For functional annotation, gene sets from org.Mm.eg.db, a genome-wide annotation package for mouse, were utilized. The analysis was performed via one-on-one comparisons of mean expression between high strain vs. reference regions and low strain vs. reference regions. Gene-set enrichment analysis was performed in one-on-one comparisons between mean expression of high strain versus reference spots and low strain versus reference spots. The significant annotation terms were selected using an FDR-adjusted p value < 0.05.

***In silico* micro-FE modelling**

Micro-FE analyses based upon the registered *in vivo* micro-CT images were used to simulate axial compression and generate tissue-scale 3D maps of the mechanical environment (*12, 77*). In brief,

the micro-CT images were cropped to dimensions of 300 x 300 x 186 voxels. All voxels were converted to linear hexahedral elements to generate an FE mesh. Grayscale values of the voxels were then converted from density (mg HA/cm^3) to Young's moduli (GPa) (*78*). Regions of soft tissue were assigned a Young's modulus of 0.003 GPa (*79*). In addition, the marrow cavity of the femur was capped on the top and bottom slices of the image stack with a plate of 20 GPa to prevent edge effects due to the presence of soft tissue. To map the mechanical environment at the fracture site, uniaxial loading was simulated by applying a 1% compressive displacement to the top slice in the axial direction whilst the bottom slice was held fixed. ParOSol - a linear micro-FE solver - was used to solve each finite element simulation and compute the mechanical environment (*80*). Effective strain, which combines both volumetric and deviatoric strains (and drives fluid movement and direct strain, respectively), represented the mechanical environment (*9*, *77*). The results of the simulation were scaled as follows:

$$\varepsilon_{actual} = \frac{F_{applied}}{F_{resultant}} \varepsilon_{simulation}$$

where $\varepsilon_{simulation}$ is the effective strain result based on the simulation of uniaxial loading, $F_{resultant}$ is the sum of the reaction forces of all the nodes of the uppermost surface, $F_{applied}$ is the cyclic loading force applied and ε_{actual} is the strain induced under the applied force (*77*).

Mechanomics

Histological sections on which spatial transcriptomics were performed were visually aligned within the 3D maps of the mechanical environment to correlate spatially resolved gene expression profiles with their local in vivo mechanical environments (ParaView version 5.7.0). Maps of the mechanical environment were sub-divided into high strain (> 1000 με) and low strain (< 500 με) regions, and the corresponding gene expression profiles were analyzed with respect to a reference strain region (> 500 με and < 1000 με).

References

1. J. Wolff, Das gesetz der transformation der knochen, berlin, a. hirchwild. *The Law of Bone Remodeling* (1892).

2. L. E. Claes, *Mechanobiology of Fracture Healing: From Basic Science to Clinical Application* (Springer International Publishing, Cham, 2022; https://link.springer.com/10.1007/978-3-030-94082-9)*SpringerBriefs in Bioengineering*.

3. S. W. Verbruggen, L. M. McNamara, "Bone mechanobiology in health and disease" in *Mechanobiology in Health and Disease* (Elsevier, 2018; https://linkinghub.elsevier.com/retrieve/pii/B9780128129524000064), pp. 157–214.

4. A. B. Castillo, J. C. Chen, C. R. Jacobs, "Cellular and molecular mechanotransduction in bone" in *Marcus and Feldman's Osteoporosis* (Elsevier, 2021; https://linkinghub.elsevier.com/retrieve/pii/B9780128130735000149), pp. 309–335.

5. G. R. Paul, A. Malhotra, R. Müller, Mechanical Stimuli in the Local In Vivo Environment in Bone: Computational Approaches Linking Organ-Scale Loads to Cellular Signals. *Curr Osteoporos Rep* **16**, 395–403 (2018).

6. M. S. Thompson, D. R. Epari, F. Bieler, G. N. Duda, *In vitro* models for bone mechanobiology: Applications in bone regeneration and tissue engineering. *Proc Inst Mech Eng H* **224**, 1533–1541 (2010).

7. Q. Ma, Z. Miri, H. J. Haugen, A. Moghanian, D. Loca, Significance of mechanical loading in bone fracture healing, bone regeneration, and vascularization. *J Tissue Eng* **14**, 204173142311725 (2023).

8. P. Christen, R. Müller, In vivo Visualisation and Quantification of Bone Resorption and Bone Formation from Time-Lapse Imaging. *Curr Osteoporos Rep* **15**, 311–317 (2017).

9. D. C. Tourolle né Betts, E. Wehrle, G. R. Paul, G. A. Kuhn, P. Christen, S. Hofmann, R. Müller, The association between mineralised tissue formation and the mechanical local in vivo environment: Time-lapsed quantification of a mouse defect healing model. *Scientific Reports* **10**, 1–10 (2020).

10. J. R. Moffitt, E. Lundberg, H. Heyn, The emerging landscape of spatial profiling technologies. *Nat Rev Genet*, doi: 10.1038/s41576-022-00515-3 (2022).

11. E. Wehrle, G. R. Paul, D. C. Tourolle né Betts, G. A. Kuhn, R. Müller, Individualized cyclic mechanical loading improves callus properties during the remodelling phase of fracture healing in mice as assessed from time-lapsed in vivo imaging. *Sci Rep* **11**, 23037 (2021).

12. G. R. Paul, E. Wehrle, D. C. Tourolle, G. A. Kuhn, R. Müller, Real-time finite element analysis allows homogenization of tissue scale strains and reduces variance in a mouse defect healing model. *Sci Rep* **11**, 13511 (2021).

13. E. Wehrle, D. Günther, N. Mathavan, A. Singh, R. Müller, Protocol for preparing formalin-fixed paraffin-embedded musculoskeletal tissue samples from mice for spatial transcriptomics. *STAR Protocols* **5**, 102986 (2024).

14. D. Song, G. He, F. Song, Z. Wang, X. Liu, L. Liao, J. Ni, M. J. Silva, F. Long, Inducible expression of Wnt7b promotes bone formation in aged mice and enhances fracture healing. *Bone Res* **8**, 4 (2020).

15. M. Horita, K. Nishida, J. Hasei, T. Furumatsu, M. Sakurai, Y. Onodera, K. Fukuda, D. M. Salter, T. Ozaki, Involvement of ADAM12 in Chondrocyte Differentiation by Regulation of TGF-β1–Induced IGF-1 and RUNX-2 Expressions. *Calcif Tissue Int* **105**, 97–106 (2019).

16. C. Ma, C. Tao, Z. Zhang, H. Zhou, C. Fan, D. Wang, Development of artificial bone graft via in vitro endochondral ossification (ECO) strategy for bone repair. *Materials Today Bio* **23**, 100893 (2023).

17. G. Zimmermann, K. H. K. Schmeckenbecher, S. Boeuf, S. Weiss, R. Bock, A. Moghaddam, W. Richter, Differential gene expression analysis in fracture callus of patients with regular and failed bone healing. *Injury* **43**, 347–356 (2012).

18. V. S. Salazar, S. Ohte, L. P. Capelo, L. Gamer, V. Rosen, Specification of osteoblast cell fate by canonical Wnt signaling requires *Bmp2*. *Development*, dev.136879 (2016).

19. G. Manickam, P. Moffatt, M. Murshed, Role of SMPD3 during bone fracture healing and regulation of its expression. *Molecular and cellular biology* (2018).

20. S. Dillon, K. A. Staines, J. L. Millán, C. Farquharson, How To Build a Bone: PHOSPHO1, Biomineralization, and Beyond. *JBMR Plus* **3**, e10202 (2019).

21. A. G. Lambi, M. Y. Harris, M. Amin, P. G. Joiner, B. A. Hilliard, S. Assari, S. N. Popoff, M. F. Barbe, Blocking CCN2 Reduces Established Bone Loss Induced by Prolonged Intense Loading by Increasing Osteoblast Activity in Rats. *JBMR Plus* **7**, e10783 (2023).

22. K. Nolan, C. Kattamuri, D. M. Luedeke, E. B. Angerman, S. A. Rankin, M. L. Stevens, A. M. Zorn, T. B. Thompson, Structure of Neuroblastoma Suppressor of Tumorigenicity 1 (NBL1). *Journal of Biological Chemistry* **290**, 4759–4771 (2015).

23. M. Julien, S. Khoshniat, A. Lacreusette, M. Gatius, A. Bozec, E. F. Wagner, Y. Wittrant, M. Masson, P. Weiss, L. Beck, D. Magne, J. Guicheux, Phosphate-Dependent Regulation of MGP in Osteoblasts: Role of ERK1/2 and Fra-1. *J of Bone & Mineral Res* **24**, 1856–1868 (2009).

24. S. Khoshniat, A. Bourgine, M. Julien, M. Petit, P. Pilet, T. Rouillon, M. Masson, M. Gatius, P. Weiss, J. Guicheux, L. Beck, Phosphate-dependent stimulation of MGP and OPN expression in osteoblasts via the ERK1/2 pathway is modulated by calcium. *Bone* **48**, 894–902 (2011).

25. A. Stubelius, A. Andersson, R. Holmdahl, C. Ohlsson, U. Islander, H. Carlsten, Ncf1 affects osteoclast formation but is not critical for postmenopausal bone loss. *BMC Musculoskelet Disord* **17**, 464 (2016).

26. L. C. Grevers, T. J. De Vries, T. Vogl, S. Abdollahi-Roodsaz, A. W. Sloetjes, P. J. M. Leenen, J. Roth, V. Everts, W. B. Van Den Berg, P. L. E. M. Van Lent, S100A8 enhances osteoclastic bone resorption in vitro through activation of Toll-like receptor 4: Implications for bone destruction in murine antigen-induced arthritis. *Arthritis & Rheumatism* **63**, 1365–1375 (2011).

27. K. B. S. Paiva, J. M. Granjeiro, "Matrix Metalloproteinases in Bone Resorption, Remodeling, and Repair" in *Progress in Molecular Biology and Translational Science* (Elsevier, 2017; https://linkinghub.elsevier.com/retrieve/pii/S1877117317300674)vol. 148, pp. 203–303.

28. L. Zhu, Y. Tang, X.-Y. Li, E. T. Keller, J. Yang, J.-S. Cho, T. Y. Feinberg, S. J. Weiss, Osteoclast-mediated bone resorption is controlled by a compensatory network of secreted and membrane-tethered metalloproteinases. *Sci. Transl. Med.* **12**, eaaw6143 (2020).

29. H. Zreiqat, C. R. Howlett, S. Gronthos, D. Hume, C. L. Geczy, S100A8/S100A9 and their association with cartilage and bone. *J Mol Hist* **38**, 381–391 (2007).

30. B. Dong, M. Hiasa, Y. Higa, Y. Ohnishi, I. Endo, T. Kondo, Y. Takashi, M. Tsoumpra, R. Kainuma, S. Sawatsubashi, H. Kiyonari, G. Shioi, H. Sakaue, T. Nakashima, S. Kato, M. Abe, S. Fukumoto, T. Matsumoto, Osteoblast/osteocyte-derived interleukin-11 regulates osteogenesis and systemic adipogenesis. *Nat Commun* **13**, 7194 (2022).

31. B. Kespohl, T. Schumertl, J. Bertrand, J. Lokau, C. Garbers, The cytokine interleukin-11 crucially links bone formation, remodeling and resorption. *Cytokine & Growth Factor Reviews* **60**, 18–27 (2021).

32. T. Nishida, S. Kubota, Roles of CCN2 as a mechano-sensing regulator of chondrocyte differentiation. *Japanese Dental Science Review* **56**, 119–126 (2020).

33. N. Holguin, M. D. Brodt, M. J. Silva, Activation of Wnt Signaling by Mechanical Loading Is Impaired in the Bone of Old Mice. *J of Bone & Mineral Res* **31**, 2215–2226 (2016).

34. R. B. Choi, A. G. Robling, The Wnt pathway: An important control mechanism in bone's response to mechanical loading. *Bone* **153**, 116087 (2021).

35. M. Semënov, K. Tamai, X. He, SOST Is a Ligand for LRP5/LRP6 and a Wnt Signaling Inhibitor. *Journal of Biological Chemistry* **280**, 26770–26775 (2005).

36. A. G. Robling, P. J. Niziolek, L. A. Baldridge, K. W. Condon, M. R. Allen, I. Alam, S. M. Mantila, J. Gluhak-Heinrich, T. M. Bellido, S. E. Harris, C. H. Turner, Mechanical Stimulation of Bone in Vivo Reduces Osteocyte Expression of Sost/Sclerostin. *Journal of Biological Chemistry* **283**, 5866–5875 (2008).

37. L. I. Plotkin, T. L. Speacht, H. J. Donahue, Cx43 and Mechanotransduction in Bone. *Curr Osteoporos Rep* **13**, 67–72 (2015).

38. R. Chen, R. Baron, F. Gori, Sfrp4 and the Biology of Cortical Bone. *Curr Osteoporos Rep* **20**, 153–161 (2022).

39. S. M. Mantila Roosa, Y. Liu, C. H. Turner, Gene expression patterns in bone following mechanical loading. *J Bone Miner Res* **26**, 100–112 (2011).

40. S. M. Mantila Roosa, Y. Liu, C. H. Turner, Alternative splicing in bone following mechanical loading. *Bone* **48**, 543–551 (2011).

41. W. Guo, P. Jin, R. Li, L. Huang, Z. Liu, H. Li, T. Zhou, B. Fang, L. Xia, Dynamic network biomarker identifies cdkn1a-mediated bone mineralization in the triggering phase of osteoporosis. *Exp Mol Med* **55**, 81–94 (2023).

42. E. A. Blaber, N. Dvorochkin, C. Lee, J. S. Alwood, R. Yousuf, P. Pianetta, R. K. Globus, B. P. Burns, E. A. C. Almeida, Microgravity Induces Pelvic Bone Loss through Osteoclastic Activity, Osteocytic Osteolysis, and Osteoblastic Cell Cycle Inhibition by CDKN1a/p21. *PLoS ONE* **8**, e61372 (2013).

43. Y. Wang, A. Nizkorodov, K. Riemenschneider, C. S. D. Lee, R. Olivares-Navarrete, Z. Schwartz, B. D. Boyan, Impaired Bone Formation in Pdia3 Deficient Mice. *PLoS ONE* **9**, e112708 (2014).

44. S. H. Mun, H. Y. Won, P. Hernandez, H. L. Aguila, S. Lee, Deletion of CD74, a putative MIF receptor, in mice enhances osteoclastogenesis and decreases bone mass. *J of Bone & Mineral Res* **28**, 948–959 (2013).

45. P. W. Gunning, E. C. Hardeman, P. Lappalainen, D. P. Mulvihill, Tropomyosin – master regulator of actin filament function in the cytoskeleton. *Journal of Cell Science*, jcs.172502 (2015).

46. B. K. McMichael, P. Kotadiya, T. Singh, L. S. Holliday, B. S. Lee, Tropomyosin isoforms localize to distinct microfilament populations in osteoclasts. *Bone* **39**, 694–705 (2006).

47. D. E. Maridas, V. E. DeMambro, P. T. Le, K. Nagano, R. Baron, S. Mohan, C. J. Rosen, IGFBP-4 regulates adult skeletal growth in a sex-specific manner. *Journal of Endocrinology* **233**, 131–144 (2017).

48. M. Zhang, M. Faugere, H. Malluche, C. J. Rosen, S. D. Chernausek, T. L. Clemens, Paracrine Overexpression of IGFBP-4 in Osteoblasts of Transgenic Mice Decreases Bone Turnover and Causes Global Growth Retardation. *J of Bone & Mineral Res* **18**, 836–843 (2003).

49. H. Moon, W. Ko, M. Jung, J. H. Kim, W. Lee, K. Park, J. Heo, J. B. Bang, I. K. Kwon, Coenzyme Q10 Regulates Osteoclast and Osteoblast Differentiation. *Journal of Food Science* **78** (2013).

50. D. Zheng, C. Cui, M. Yu, X. Li, L. Wang, X. Chen, Y. Lin, Coenzyme Q10 promotes osteoblast proliferation and differentiation and protects against ovariectomy-induced osteoporosis. *Mol Med Report*, doi: 10.3892/mmr.2017.7907 (2017).

51. S. Jo, S. H. Lee, C. Jeon, H.-R. Jo, Y. J. You, J. K. Lee, I.-H. Sung, T.-H. Kim, C.-H. Lee, Myosin heavy chain 2 (MYH2) expression in hypertrophic chondrocytes of soft callus provokes endochondral bone formation in fracture. *Life Sciences* **334**, 122204 (2023).

52. M. Fukuda, T. Yoshizawa, Md. F. Karim, S. U. Sobuz, W. Korogi, D. Kobayasi, H. Okanishi, M. Tasaki, K. Ono, T. Sawa, Y. Sato, M. Chirifu, T. Masuda, T. Nakamura, H. Tanoue, K. Nakashima, Y. Kobashigawa, H. Morioka, E. Bober, S. Ohtsuki, Y. Yamagata, Y. Ando, Y. Oike, N. Araki, S. Takeda, H. Mizuta, K. Yamagata, SIRT7 has a critical role in bone formation by regulating lysine acylation of SP7/Osterix. *Nat Commun* **9**, 2833 (2018).

53. J. Gao, Z. Feng, X. Wang, M. Zeng, J. Liu, S. Han, J. Xu, L. Chen, K. Cao, J. Long, Z. Li, W. Shen, J. Liu, SIRT3/SOD2 maintains osteoblast differentiation and bone formation by regulating mitochondrial stress. *Cell Death Differ* **25**, 229–240 (2018).

54. K. Maruyama, M. Fukasaka, A. Vandenbon, T. Saitoh, T. Kawasaki, T. Kondo, K. K. Yokoyama, H. Kidoya, N. Takakura, D. Standley, O. Takeuchi, S. Akira, The Transcription Factor Jdp2 Controls Bone Homeostasis and Antibacterial Immunity by Regulating Osteoclast and Neutrophil Differentiation. *Immunity* **37**, 1024–1036 (2012).

55. Y. Chen, T. Gridley, Compensatory regulation of the *Snai1* and *Snai2* genes during chondrogenesis. *J of Bone & Mineral Res* **28**, 1412–1421 (2013).

56. C. A. De Frutos, R. Dacquin, S. Vega, P. Jurdic, I. Machuca-Gayet, M. Angela Nieto, Snail1 controls bone mass by regulating Runx2 and VDR expression during osteoblast differentiation. *EMBO J* **28**, 686–696 (2009).

57. H. Kanzaki, A. Movila, R. Kayal, M. H. Napimoga, K. Egashira, F. Dewhirst, H. Sasaki, M. Howait, A. Al-dharrab, A. Mira, X. Han, M. A. Taubman, F. C. Nichols, T. Kawai, Phosphoglycerol dihydroceramide, a distinctive ceramide produced by Porphyromonas gingivalis, promotes RANKL-induced osteoclastogenesis by acting on non-muscle myosin II-A (Myh9), an osteoclast cell fusion regulatory factor. *Biochimica et Biophysica Acta (BBA) - Molecular and Cell Biology of Lipids* **1862**, 452–462 (2017).

58. B. K. McMichael, R. B. Wysolmerski, B. S. Lee, Regulated Proteolysis of Nonmuscle Myosin IIA Stimulates Osteoclast Fusion. *Journal of Biological Chemistry* **284**, 12266–12275 (2009).

59. S. Ehnert, A.-K. Fentz, A. Schreiner, J. Birk, B. Wilbrand, P. Ziegler, M. K. Reumann, H. Wang, K. Falldorf, A. K. Nussler, Extremely low frequency pulsed electromagnetic fields cause antioxidative defense mechanisms in human osteoblasts via induction of •O2 − and H2O2. *Sci Rep* **7**, 14544 (2017).

60. C. D. Kegelman, D. E. Mason, J. H. Dawahare, D. J. Horan, G. D. Vigil, S. S. Howard, A. G. Robling, T. M. Bellido, J. D. Boerckel, Skeletal cell YAP and TAZ combinatorially promote bone development. *FASEB j.* **32**, 2706–2721 (2018).

61. A. L. Jacob, C. Smith, J. Partanen, D. M. Ornitz, Fibroblast growth factor receptor 1 signaling in the osteo-chondrogenic cell lineage regulates sequential steps of osteoblast maturation. *Developmental Biology* **296**, 315–328 (2006).

62. Y. Tang, P. Yang, M. Jin, S. Huang, H. Chen, L. Chen, J. Yang, N. Su, Fgfr1 deficiency in osteocytes leads to increased bone mass by enhancing Wnt/β-catenin signaling. *Bone* **174**, 116817 (2023).

63. X. Lu, N. Su, J. Yang, W. Huang, C. Li, L. Zhao, Q. He, X. Du, Y. Shen, B. Chen, L. Chen, Fibroblast growth factor receptor 1 regulates the differentiation and activation of osteoclasts through Erk1/2 pathway. *Biochemical and Biophysical Research Communications* **390**, 494–499 (2009).

64. J. H. Park, E. Jeong, J. Lin, R. Ko, J. H. Kim, S. Yi, Y. Choi, I.-C. Kang, D. Lee, S. Y. Lee, RACK1 interaction with c-Src is essential for osteoclast function. *Exp Mol Med* **51**, 1–9 (2019).

65. N. Mathavan, G. R. Paul, F. C. Marques, D. Yilmaz, G. A. Kuhn, E. Wehrle, R. Muller, "Individualized cyclic mechanical loading significantly augments the regenerative response of bone in a mouse model of premature aging" (WILEY 111 RIVER ST, HOBOKEN 07030-5774, NJ USA, 2022)vol. 37, pp. 339–340.

66. D. Yılmaz, N. Mathavan, E. Wehrle, G. A. Kuhn, R. Müller, Mouse models of accelerated aging in musculoskeletal research for assessing frailty, sarcopenia, and osteoporosis – A review. *Ageing Research Reviews* **93**, 102118 (2024).

67. N. Mathavan, L. Gregorio, D. Yilmaz, F. C. Marques, G. A. Kuhn, R. Müller, E. Wehrle, Evaluation of a CRISPR/Cas9-based dual-fluorescent reporter mouse model of premature aging to investigate the mechanobiology of bone regeneration. *Bone Reports* **16**, 101349 (2022).

68. T. Kon, T. Cho, T. Aizawa, M. Yamazaki, N. Nooh, D. Graves, L. C. Gerstenfeld, T. A. Einhorn, Expression of Osteoprotegerin, Receptor Activator of NF-κB Ligand (Osteoprotegerin Ligand) and Related Proinflammatory Cytokines During Fracture Healing. *J of Bone & Mineral Res* **16**, 1004–1014 (2001).

69. A. G. Robling, L. F. Bonewald, The Osteocyte: New Insights. *Annu. Rev. Physiol.* **82**, 485–506 (2020).

70. T. Bellido, A. A. Ali, I. Gubrij, L. I. Plotkin, Q. Fu, C. A. O'Brien, S. C. Manolagas, R. L. Jilka, Chronic Elevation of Parathyroid Hormone in Mice Reduces Expression of Sclerostin by Osteocytes: A Novel Mechanism for Hormonal Control of Osteoblastogenesis. *Endocrinology* **146**, 4577–4583 (2005).

71. D. C. Genetos, C. E. Yellowley, G. G. Loots, Prostaglandin E2 Signals Through PTGER2 to Regulate Sclerostin Expression. *PLoS ONE* **6**, e17772 (2011).

72. B. A. Coates, J. A. McKenzie, E. G. Buettmann, X. Liu, P. M. Gontarz, B. Zhang, M. J. Silva, Transcriptional profiling of intramembranous and endochondral ossification after fracture in mice. *Bone* **127**, 577–591 (2019).

73. B. Kruck, E. A. Zimmermann, S. Damerow, C. Figge, C. Julien, D. Wulsten, T. Thiele, M. Martin, R. Hamdy, M. K. Reumann, G. N. Duda, S. Checa, B. M. Willie, Sclerostin Neutralizing Antibody Treatment Enhances Bone Formation but Does Not Rescue Mechanically Induced Delayed Healing. *J of Bone & Mineral Res* **33**, 1686–1697 (2018).

74. X. Xiao, C. Juan, T. Drennon, C. R. Uytingco, N. Vishlaghi, D. Sokolowskei, L. Xu, B. Levi, M. C. Sammarco, R. J. Tower, Spatial transcriptomic interrogation of the murine bone marrow signaling landscape. *Bone Res* **11**, 59 (2023).

75. D. Yılmaz, F. Correia Marques, Y. Fischer, S. Zimmermann, G. Hwang, P. R. Atkins, N. Mathavan, A. Singh, P. C. De Souza, G. A. Kuhn, E. Wehrle, R. Müller, "Unraveling the Mechano-Molecular Mechanisms of TRAP Activity Using CRISPR/Cas9 Mediated Fluorescent Reporter Mice" (preprint, SSRN, 2023); https://doi.org/10.2139/ssrn.4476675.

76. K. Van Den Berge, F. Perraudeau, C. Soneson, M. I. Love, D. Risso, J.-P. Vert, M. D. Robinson, S. Dudoit, L. Clement, Observation weights unlock bulk RNA-seq tools for zero inflation and single-cell applications. *Genome Biol* **19**, 24 (2018).

77. G. R. Paul, P. Vallaster, M. Rüegg, A. C. Scheuren, D. C. Tourolle, G. A. Kuhn, E. Wehrle, R. Müller, Tissue-Level Regeneration and Remodeling Dynamics are Driven by Mechanical Stimuli in the Microenvironment in a Post-Bridging Loaded Femur Defect Healing Model in Mice. *Front. Cell Dev. Biol.* **10**, 856204 (2022).

78. L. Mulder, J. H. Koolstra, J. M. J. Den Toonder, T. M. G. J. Van Eijden, Intratrabecular distribution of tissue stiffness and mineralization in developing trabecular bone. *Bone* **41**, 256–265 (2007).

79. U. Simon, P. Augat, M. Utz, L. Claes, A numerical model of the fracture healing process that describes tissue development and revascularisation. *Computer Methods in Biomechanics and Biomedical Engineering* **14**, 79–93 (2011).

80. C. Flaig, P. Arbenz, A scalable memory efficient multigrid solver for micro-finite element analyses based on CT images. *Parallel Computing* **37**, 846–854 (2011).

Acknowledgments

The authors gratefully acknowledge the ETH Phenomics Centre (EPIC) of ETH Zürich, and particularly Susanne Freedrich, for assistance with the *in vivo* experiments.

Spatial transcriptomics was performed at the Functional Genomics Center Zürich (FGCZ) of the University of Zürich and ETH Zürich.

Tissue processing and paraffin embedding were performed at ScopeM at ETH Zürich.

Sectioning, staining and imaging were performed at ScopeM at ETH Zürich and at the Institute of Pathology and Molecular Pathology at the Universitäts Spital Zürich (USZ).

Dr. Graeme Paul for his contributions in composing Figure 1.

Funding:

European Research Council - Horizon 2020 grant ERC-2016-ADG-741883

European Union Marie Skłodowska-Curie Actions - Horizon 2020 grant 101029062

MechanoHealing-MSCA-IF-2020

Swiss National Science Foundation (IZCOZ0_198152/1, COST Action GEMSTONE)

Author contributions:

Conceptualization: NM, EW, RM

Methodology: NM, DG, EW, RM

Investigation: NM, GK, EW, RM

Analysis: NM, AS, FCM

Supervision: EW, RM

Visualization: NM, AS

Writing—original draft: NM

Writing—review & editing: All.

Competing interests: Authors declare that they have no competing interests.

Data and materials availability:

All data needed to evaluate the conclusions in the paper are present in the paper and/or the Supplementary Materials. Original spatial transcriptomics data generated for this article has been deposited in the Gene Expression Omnibus (GEO) database (accession code to be updated).

Figures and Tables

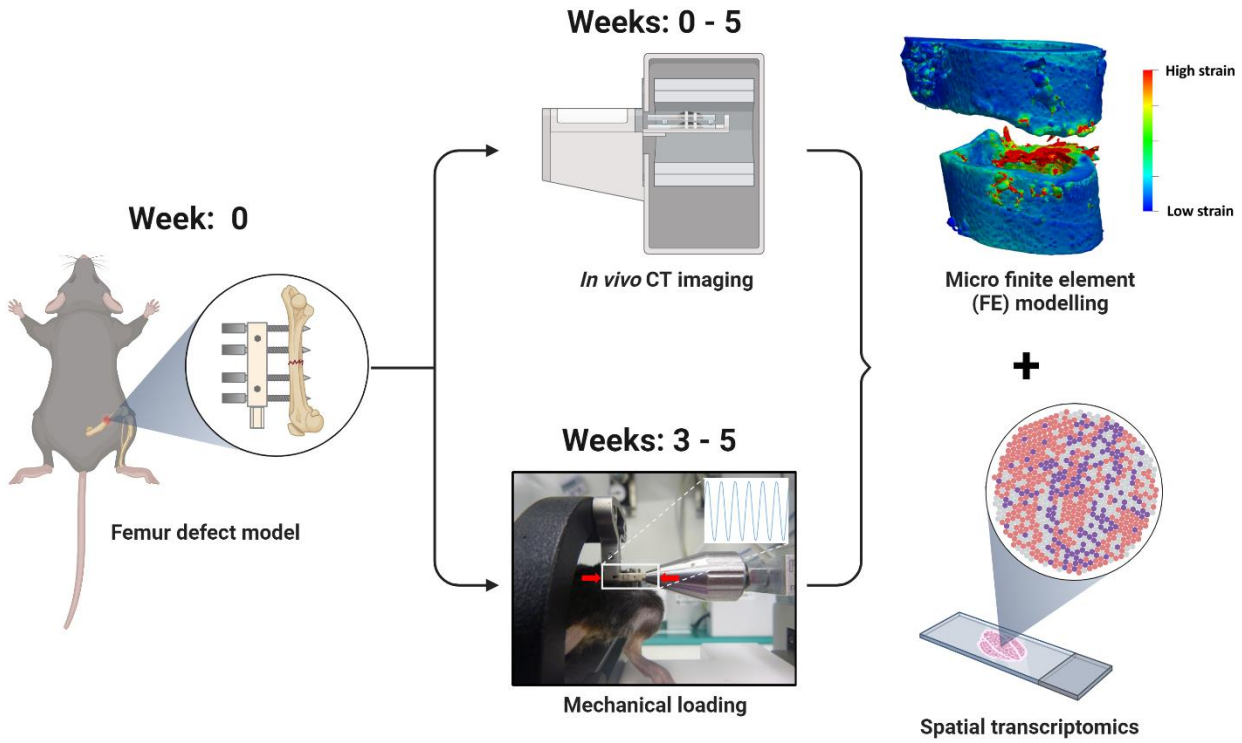

Fig. 1. Overview of our spatial transcriptomics-based "mechanomics" platform to investigate the mechanobiology of bone regeneration. At Week 0, mid-diaphyseal femoral osteotomies are introduced in the right femur of mice and stabilized with an external fixator. Time-lapsed *in vivo* micro-CT imaging is performed weekly at the fracture site (weeks 0-5; 10.5 μm resolution). Mice which exhibit bridging at 3 weeks post-surgery are subdivided into Loaded and Control groups. At weeks 3 – 5, mice received individualized cyclic loading (up to 16N) or 0N sham-loading three times per week. All mice are euthanized at 5 weeks post-surgery. Spatial transcriptomics analyses are performed on explanted femurs. Micro-FE analyses based upon *in vivo* micro-CT images are used to generate tissue-scale 3D maps of the mechanical environment. To associate spatially resolved molecular profiles of cells with their local *in vivo* mechanical environment, the spatial transcriptomics histology section is visually aligned within the 3D map of their mechanical environment. Illustration created with BioRender.

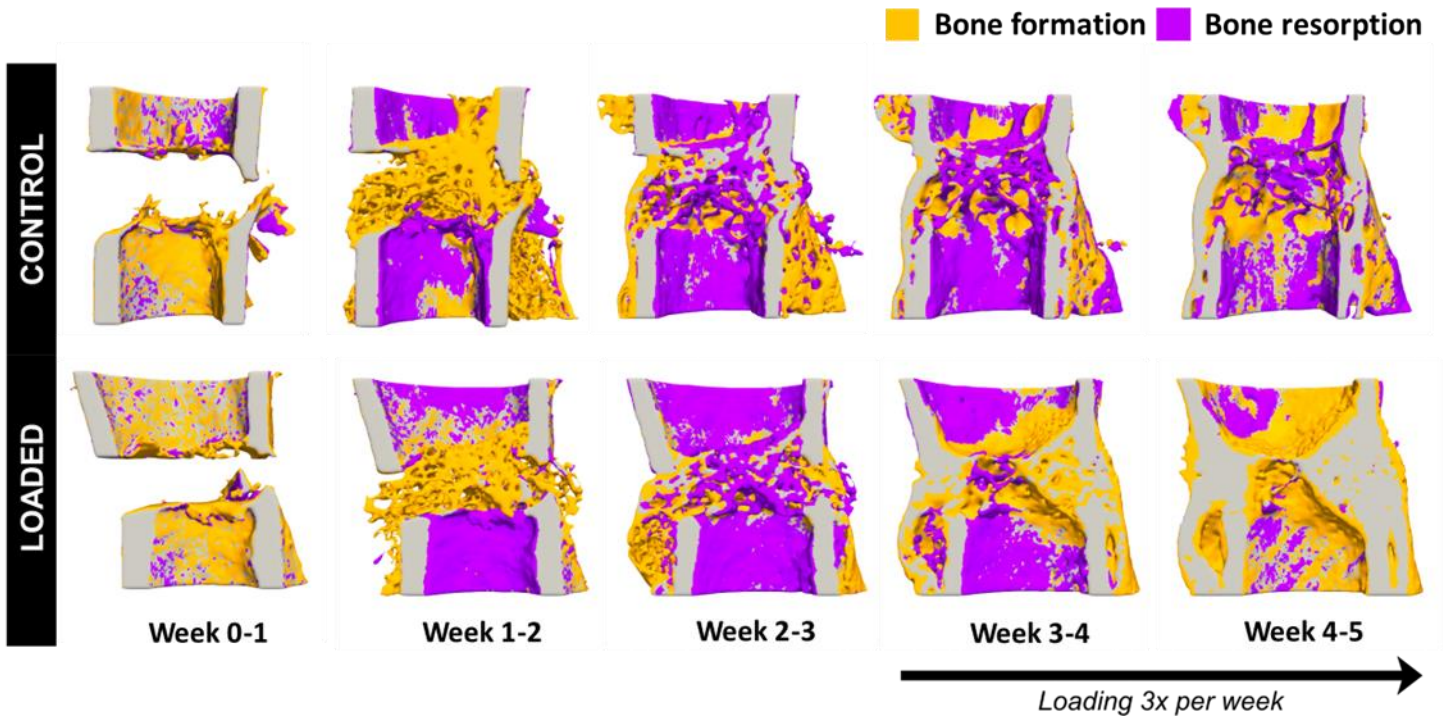

Fig. 2. Visualization of sites of bone formation, quiescence and resorption in Control and Loaded fracture sites. Sites of bone formation (orange) and bone resorption (purple) are identified via registration of time-lapsed *in vivo* images in representative samples (threshold: 395 mg HA/cm^3). In Loaded fracture sites, loading was applied 3x per week from Week 3 onwards. Visualization performed using Paraview (version 5.7.0).

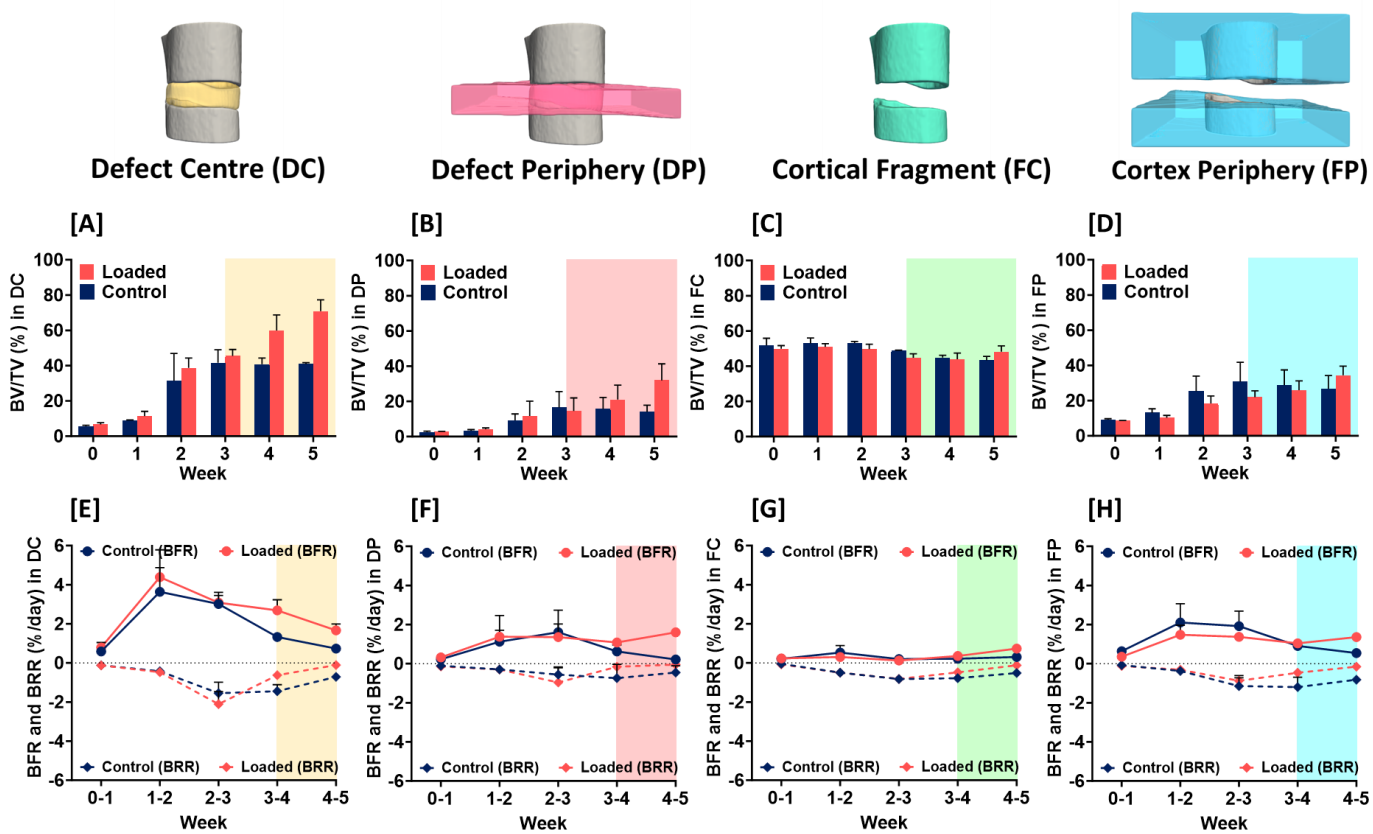

Fig. 3. *In vivo* micro-CT morphometric analysis. Quantitative morphometric analyses (n = 2 per group) were performed in four volumes of interest: the defect center (DC), the defect periphery (DP), the existing fracture cortex and medullary cavity (FC) and the cortex periphery (FP). Two parameters are presented: **[A] – [D]**: BV/TV where the bone volume (BV) is normalized to TV (DC for DC and DP, FC for FC and FP). **[E] – [H]**: bone formation rates (BFR) and bone resorption rates (BRR).

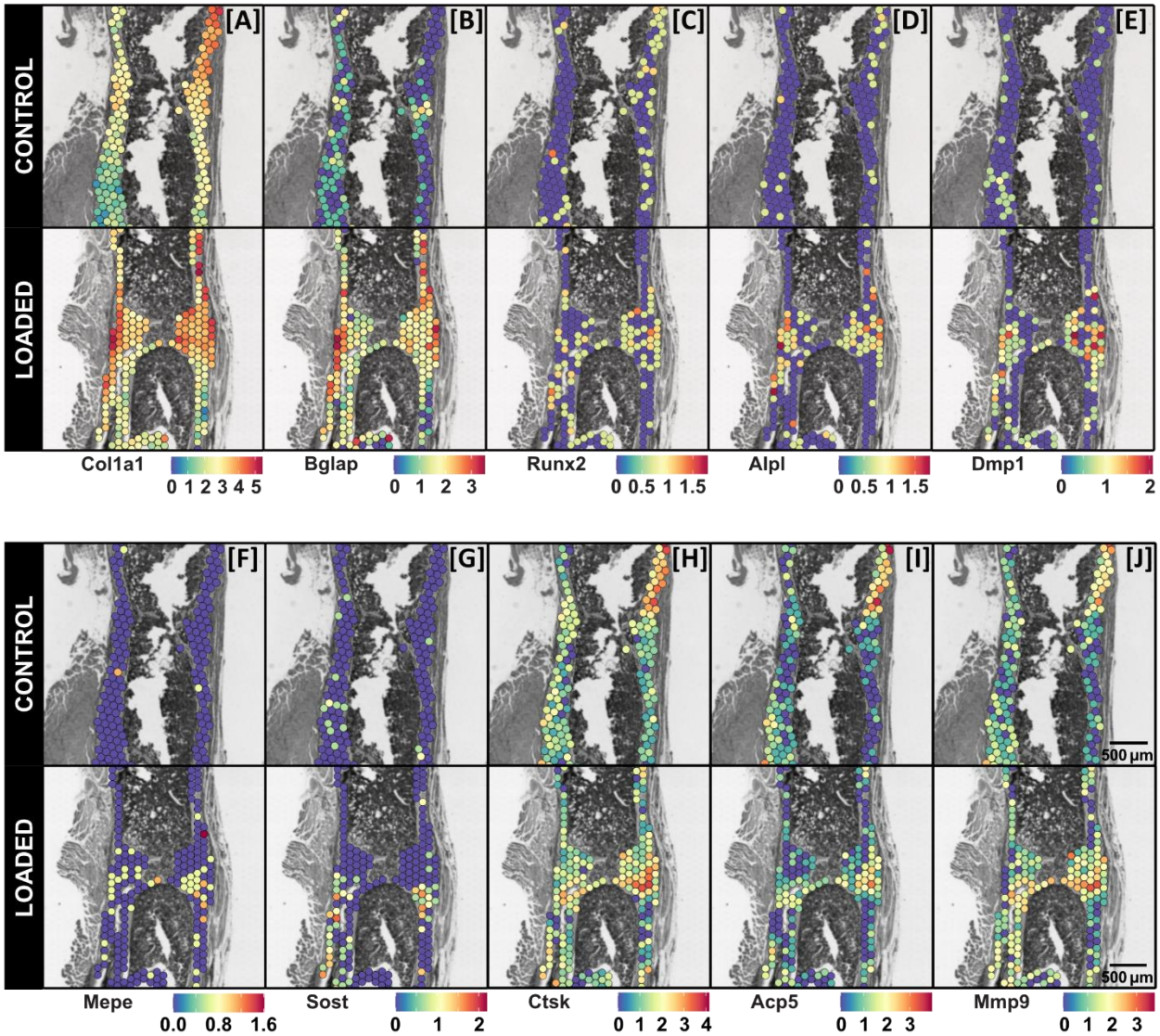

Fig. 4. Spatial gene expression maps of selected bone cell markers at the fracture site of Control and Loaded mice. Visualization of the spatial expression patterns of osteoblast markers: **[A]** *Col1a1*, **[B]** *Bglap*, **[C]** *Runx2*, **[D]** *Alpl*, osteocyte markers: **[E]** *Dmp1*, **[F]** *Mepe*, **[G]** *Sost*, and osteoclast markers: **[H]** *Ctsk*, **[I]** *Acp5*, **[J]** *Mmp9*, within the fracture sites of Control and Loaded mice are presented. Each legend denotes the normalized expression of each gene.

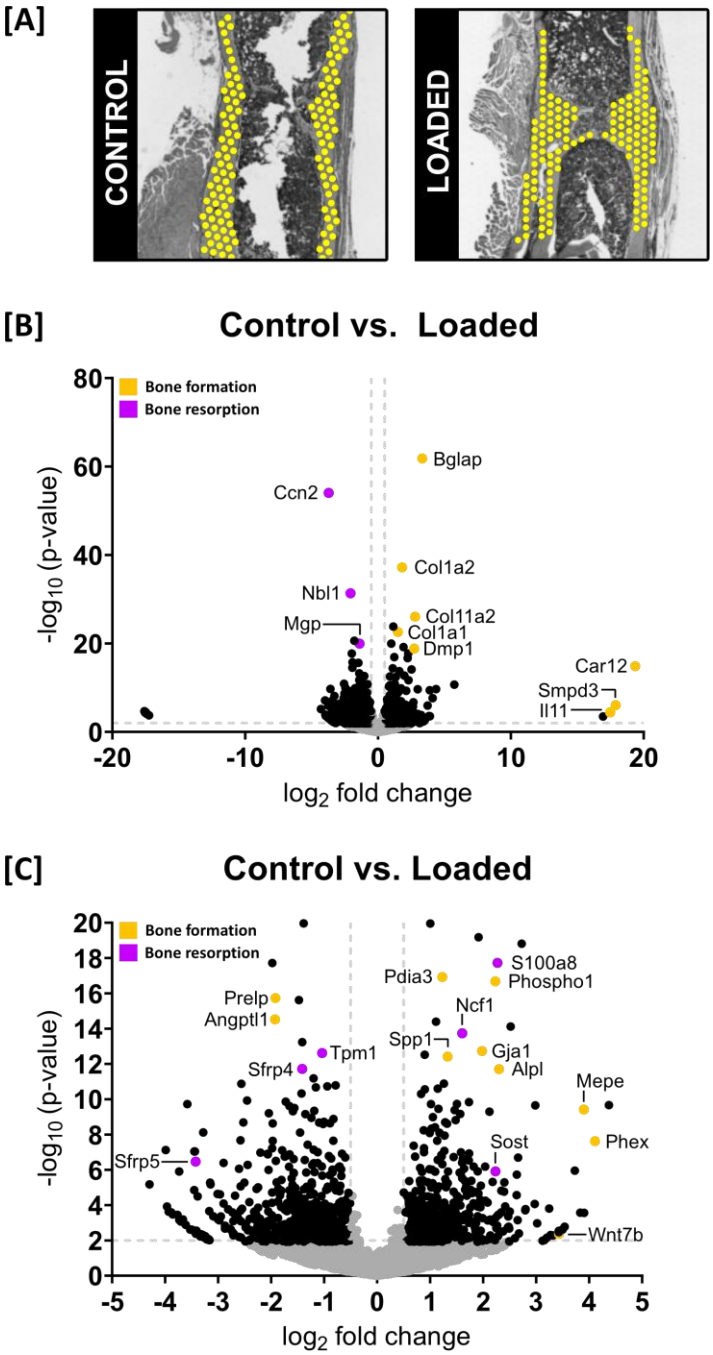

Fig. 5. Gene expression profiling in Control vs. Loaded fracture sites. [A]: Areas of interest defined in each fracture site for the analysis. **[B]**: Volcano plot to visualize differentially expressed genes (DEGs) (significance criteria: FDR-adjusted p value cutoff < 0.1 and an absolute log2 fold change > 0.5). Significant DEGs associated with bone formation are identified in orange and significant DEGs associated with bone resorption (or are inhibitors / antagonists of bone formation) are identified in purple. Non-DEGs are represented in gray. **[C]**: Magnified view of volcano plot to highlight DEGs of interest.

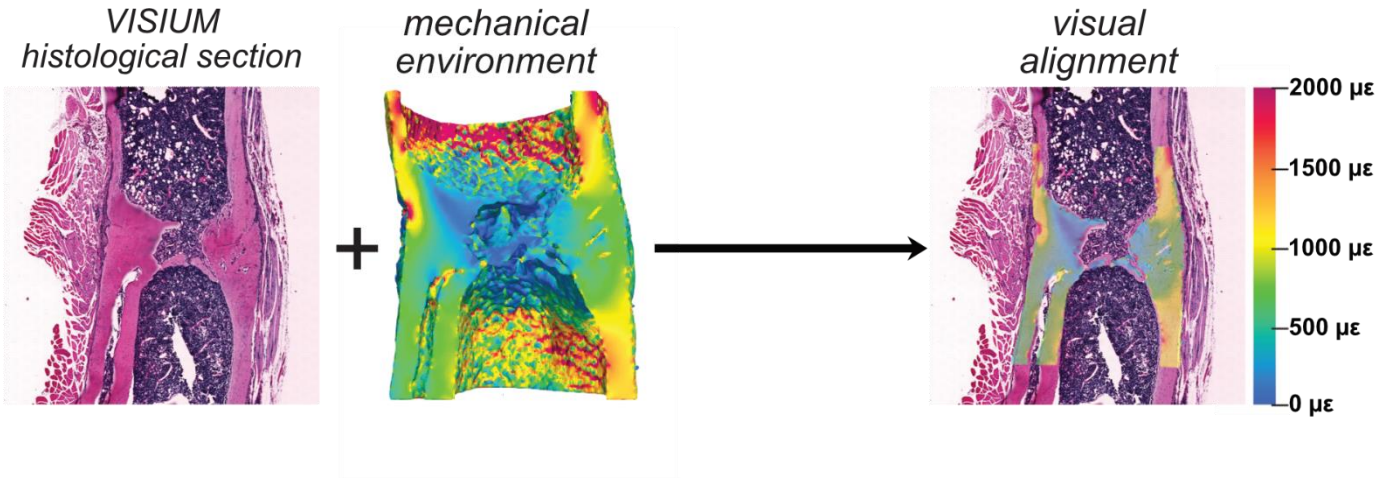

Fig. 6. Association of spatially resolved molecular profiles of cells with their local *in vivo* mechanical environment. Visual alignment of the 2D spatial transcriptomics histological section within the 3D mechanical environment in the Loaded fracture site.

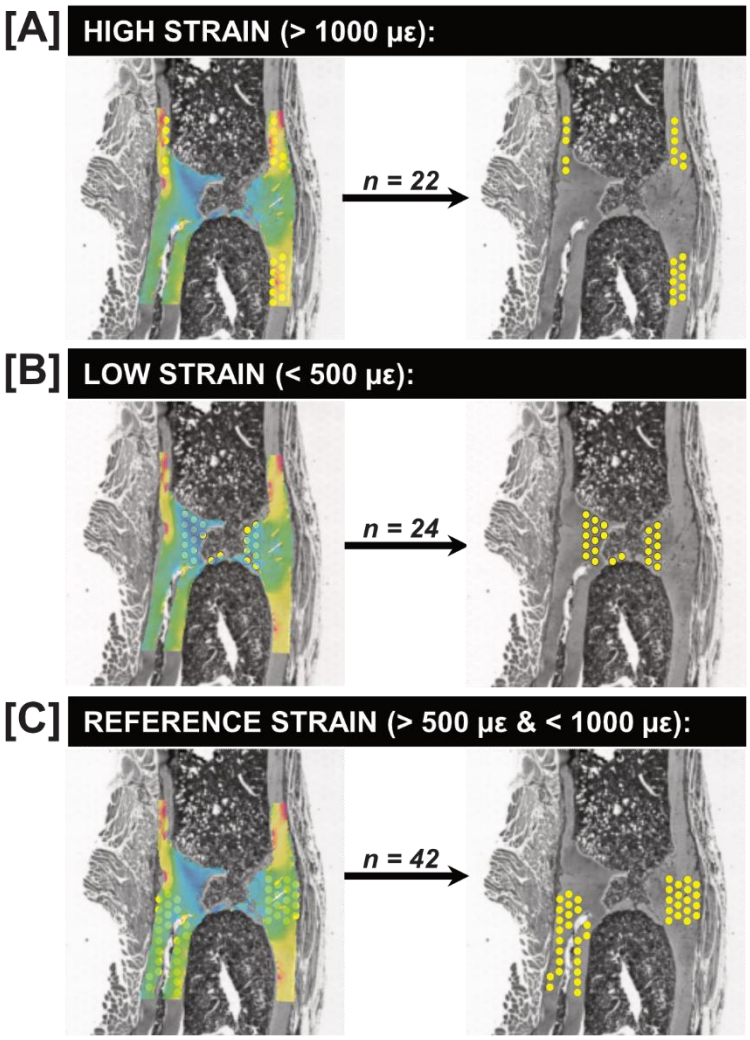

Fig. 7. Classification of spots with respect to their local *in vivo* mechanical environment. Identification of transcriptomic responses at **[A]** sites of high strain (> 1000 με), **[B]** sites of low strain (< 500 με), and **[C]** sites corresponding to a reference strain region (> 500 με and < 1000 με).

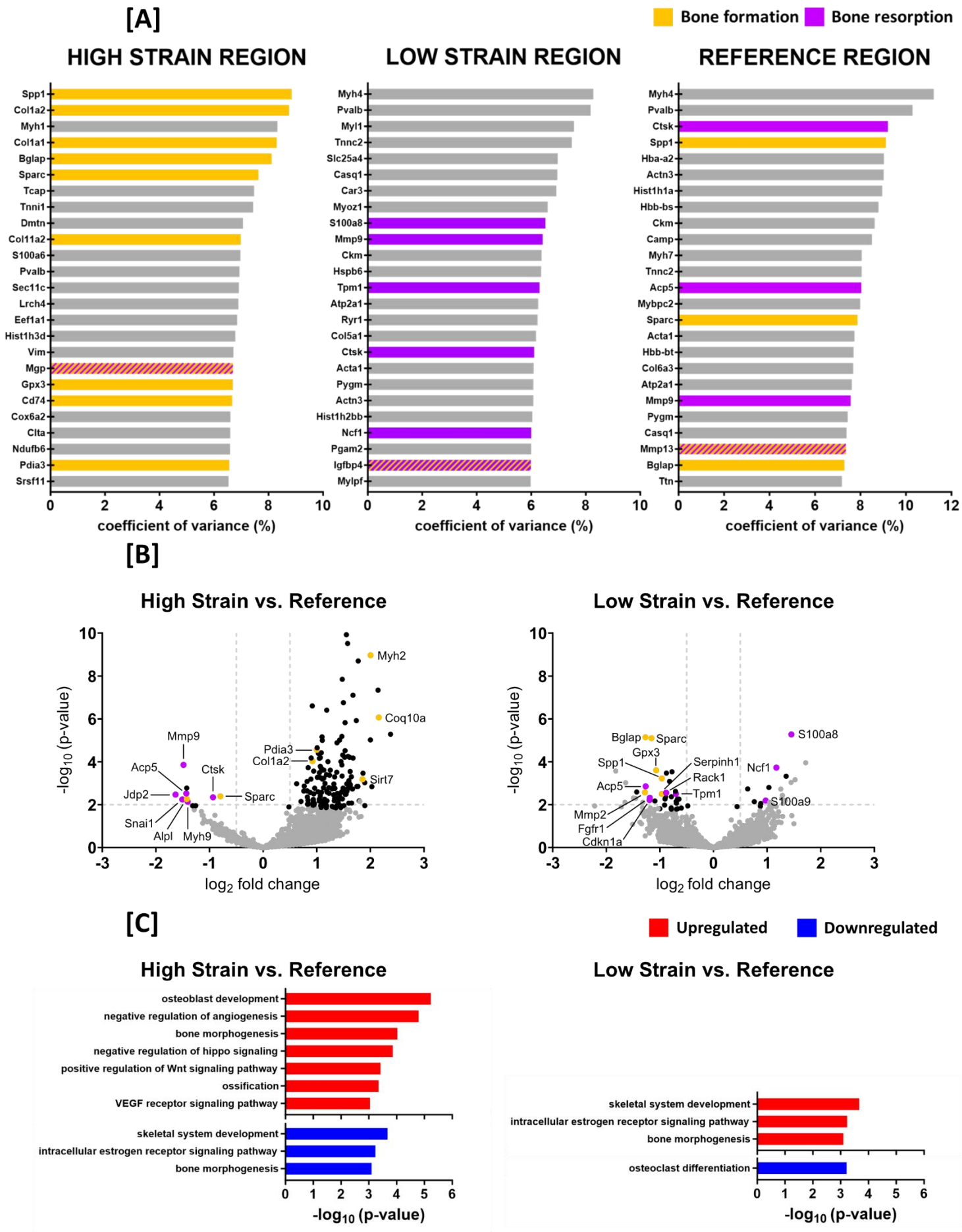
[A]
Bone formation
Bone resorption
HIGH STRAIN REGION
LOW STRAIN REGION
REFERENCE REGION
Spp1
Col1a2
Myh1
Col1a1
Bglap
Sparc
Tcap
Tnni1
Dmtn
Col11a2
S100a6
Pvalb
Sec11c
Lrch4
Eef1a1
Hist1h3d
Vim
Mgp
Gpx3
Cd74
Cox6a2
Clta
Ndufb6
Pdia3
Srsf11
Myh4
Pvalb
Myl1
Tnnc2
Slc25a4
Casq1
Car3
Myoz1
S100a8
Mmp9
Ckm
Hspb6
Tpm1
Atp2a1
Ryr1
Col5a1
Ctsk
Acta1
Pygm
Actn3
Hist1h2bb
Ncf1
Pgam2
Igfbp4
Mylpf
Myh4
Pvalb
Ctsk
Spp1
Hba-a2
Actn3
Hist1h1a
Hbb-bs
Ckm
Camp
Myh7
Tnnc2
Acp5
Mybpc2
Sparc
Acta1
Hbb-bt
Col6a3
Atp2a1
Mmp9
Pygm
Casq1
Mmp13
Bglap
Ttn
0 2 4 6 8 10
0 2 4 6 8 10
0 2 4 6 8 10 12
coefficient of variance (%)
coefficient of variance (%)
coefficient of variance (%)
[B]
High Strain vs. Reference
Low Strain vs. Reference
-log10 (p-value)
log2 fold change
Myh2
Coq10a
Mmp9
Pdia3
Col1a2
Acp5
Ctsk
Sirt7
Jdp2
Sparc
Snai1
Alpl
Myh9
Bglap
Sparc
Gpx3
S100a8
Spp1
Serpinh1
Ncf1
Rack1
Acp5
Tpm1
S100a9
Mmp2
Fgfr1
Cdkn1a
[C]
Upregulated
Downregulated
High Strain vs. Reference
Low Strain vs. Reference
osteoblast development
negative regulation of angiogenesis
bone morphogenesis
negative regulation of hippo signaling
positive regulation of Wnt signaling pathway
ossification
VEGF receptor signaling pathway
skeletal system development
intracellular estrogen receptor signaling pathway
bone morphogenesis
skeletal system development
intracellular estrogen receptor signaling pathway
bone morphogenesis
osteoclast differentiation
-log10 (p-value)
-log10 (p-value)

Fig. 8. Analysis of transcriptomic responses of cells with respect to their local *in vivo* mechanical environment. [A]: Use of the co-efficient of variance (CV) to identify the top 25 genes of functional significance within each strain region. **[B]**: Volcano plots to visualize differentially expressed genes (DEGs) between strain regions. (significance criteria: FDR-adjusted p value cutoff < 0.1 and an absolute log2 fold change > 0.5). Significant DEGs associated with bone formation are identified in orange and significant DEGs associated with bone resorption are identified in purple. Non-DEGs are represented in gray. [C]: Gene-set enrichment analysis performed in one-on-one comparisons between mean expression of high strain versus reference spots and low strain versus reference spots. The significant annotation terms were selected using an FDR-adjusted p value < 0.05. Only annotation terms relevant to bone regeneration are presented.

Supplementary Materials

Supplementary Table 1. Barcodes corresponding to all spots of the Control and Loaded bone fracture sites.

Supplementary Table 2. Differential gene expression analyses (DEG) between Control and Loaded fracture sites.

Supplementary Table 3. Differential gene expression (DEG) analysis of high strain region with respect to reference region.

Supplementary Table 4. Differential gene expression (DEG) analysis of low strain region with respect to reference region.

Supplementary Table 5. Gene-set enrichment analysis between mean expression of high strain versus reference strain regions.

Supplementary Table 6. Gene-set enrichment analysis between mean expression of low strain versus reference strain regions.